

## Computational analysis of heat transfer and fluid flow characteristics over flat bars of different heights

Y. Menni <sup>\*</sup>, A. Azzi <sup>†</sup> and C. Zidani

Unité de Recherche en Matériaux et Energies Renouvelables, URMER  
Département de Physique, Faculté des Sciences, Université Abou Bakr Belkaid,  
B.P. 119, 13000 Tlemcen, Algeria

(reçu le 09 Juillet 2015 - accepté le 30 Juillet 2016)

**Résumé** - Cette étude porte sur l'analyse computationnelle de l'écoulement turbulent et du transfert de chaleur par convection forcée à l'intérieur d'un canal bidimensionnel de section rectangulaire, muni des barres identiques, solides, planes, transversales, détachées et disposées en série sur la direction axiale de la conduite. Le fluide (air) est considéré, Newtonien, incompressible à des propriétés constantes. Le régime d'écoulement est considéré permanent et purement turbulent. Le nombre de Reynolds basé sur le diamètre hydraulique du canal est pris variable de 10.000 jusqu'à 25.000. Les équations gouvernantes, basées sur le modèle de turbulence k- $\epsilon$  standard, sont résolues par la méthode des volumes finis à l'aide de l'algorithme Simplec en utilisant le code du Calcul Numérique en Dynamique des Fluides, Fluent 6.3. En particulier, les champs et les profils de vitesse axiale, les coefficients de transfert de chaleur local et moyen, ainsi que la perte de pression ont été examinés le long du canal à condition de température des parois constante. Les paramètres de l'étude numérique sont le nombre de Reynolds et la taille des barres. Les résultats révèlent essentiellement que la taille des barres planes peut changer substantiellement les caractéristiques d'écoulement d'air et du transfert de chaleur convectif. Les mesures numériques montrent que l'augmentation de la hauteur des barres provoque une augmentation substantielle de la vitesse de fluide et du transfert de chaleur, mais la perte de charge est également très importante pour tous nombres de Reynolds utilisés.

**Abstract** - A computational analysis of steady state turbulent forced convection flow in a two-dimensional isothermal-wall rectangular channel provided by detached solid flat bars with the same cross-sectional areas in a tandem arrangement is carried out in the present work. The fluid (air) is considered, Newtonian, incompressible with constant properties. The Reynolds number based on the hydraulic diameter of the channel is varied between 10.000 and 25.000. The governing equations are solved by the Finite Volumes Method and the Simplec-algorithm, in two dimensions, employing the Commercial CFD software Fluent 6.3 with the k- $\epsilon$  standard model to describe the turbulence. In particular, fields and profiles of axial velocity, local and average heat transfer coefficients as well as pressure loss were examined along the channel at constant wall temperature condition along the top and bottom walls. The parameters of the numerical study are the Reynolds number and the flat bar size. The results reveal essentially, that the size of the bars can alter substantially the airflow and convective heat transfer characteristics. The numerical data indicates that an increase in the bar height causes a substantial increase in the Nusselt number but the pressure loss is very significant for all Reynolds numbers used.

**Keywords:** Forced convection - Pressure loss - Complex geometry - Flat bars - CFD.

---

<sup>\*</sup> menniyounes@gmail.com

<sup>†</sup> a\_azzi@mail.univ-tlemcen.dz , czidani10@yahoo.fr

## 1. INTRODUCTION

Heat transfer enhancement over bluff bodies, known as turbulence promoters, in complex geometries at low and high Reynolds number has been a major subject of intensive research over the years.

It has numerous engineering applications such as cooling of electronic components, internal cooling inside turbine blades, labyrinth shaft seals, compact heat exchangers, air-cooled solar collectors, aerodynamic fields, laser curtain seals, biomedical devices, etc. Therefore, several investigations have studied heat transfer enhancement from detached bluff bodies, in this context, in order to optimize their size, their arrangement and their shape.

The uses of bluff bodies in the cooling channel or channel heat exchanger such as flat plates or bars are often introduced in order to increase the convective heat transfer rate leading to the compact heat exchanger and increasing the efficiency. Behavior of the turbulent heat transfer and friction loss in a rectangular duct with ribs detached from one wall was studied by Liou *et al.* [1], using laser holographic interferometer and pressure measurements. The investigated flow was periodic in space both hydro-dynamically and thermally. The parameters of the experimental work were the clearance ratio ( $C/H$ ) and Reynolds number ( $Re$ ). They concluded in their experiment that the detached ribbed geometry has the advantage of eliminating the hot spots behind the attached ribs. Optimal clearance ratios for heat transfer enhancement between the present periodic detached ribs and previous single detached cylinder were also compared.

Furthermore, compact heat transfer and friction correlations were developed for a detached ribbed duct for the first time. The characteristics of the spatially periodic turbulent heat transfer and friction in a rectangular passage with perforated rectangular ribs detached from one wall were studied by Liou *et al.* [2], using laser holographic interferometer, smoke-streak flow visualization, and pressure probing for rib-to-duct hydraulic diameter ratios ( $H/D_e$ ) of 0.081, 0.106, and 0.162 and Reynolds number ( $Re$ ) range of  $5 \times 10^3 - 5 \times 10^4$ . They showed that the thermal performance of the detached solid-type ribs is found to be superior to that of the detached perforated-type ribs and the physical reason for the difference is addressed. An experimental study of turbulent heat transfer characteristics in a rectangular duct roughened by arrays of alternate attached and detached ribs was conducted by Tsia *et al.* [3].

The experiment focused on the influence of Reynolds number and rib pitch-to-height ratio on the local and average heat transfer coefficients, and pressure drop measurements. The data indicated that the entrance distance for the composite ribbed duct is longer than that for the fully-attached and detached ribbed ducts. They demonstrated that the composite ribbed wall yields the highest fully developed heat transfer coefficient, and moderate pressure-drop penalty among the three types of ribbed walls. Their results also showed that the performance evaluation under the constant pumping-power constraint showed that the composite-ribbed duct performs best of the three ribbed configurations. In general, semi-empirical correlations for friction and heat transfer in composite-ribbed ducts were developed to account for rib spacing and flow Reynolds number. Numerical investigations on turbulent flow friction and heat transfer enhancement in ducts or channels with square or rectangular bars have been carried out extensively.

Alvarez *et al.* [4] investigated the effects of two square bars placed in various arrangements in a channel on pressure drop and heat transfer by using the  $k-\epsilon$

turbulence model. Tandem arrangements and the two bars arranged side by side to the approaching flow were considered. The separation distance between the bars in both types of arrangements on the average and local heat transfer coefficients were also reported. They found that the local and global Nusselt numbers on the channel walls are strongly increased by the unsteady vortex shedding induced by the bars. Computations were conducted by Valencia [5] to study the heat transfer and friction in a channel with a mounted square bar of different sizes detached from the channel wall.

The channel walls were subjected to a constant wall temperature. The investigations revealed that the local and global Nusselt numbers on the channel walls are strongly modified by the unsteady vortex shedding induced by the bar. They also revealed that the displacement of the bar from the channel axis toward the wall did not cause an increase in the global heat transfer coefficient on the channel walls compared with the bar centered in the channel.

Other numerical study was carried out by Valencia [6] to analyze the unsteady laminar flow and heat transfer characteristics in a plane channel with two square bars mounted staggered to the approaching flow. The effect of longitudinal and transverse separation distances between the bars on the heat transfer enhancement was studied in detail. He reported that the flow structure is affected by the presence of these bars, resulting in the formation of vortices downstream from each bar. He also showed that for the cases with  $L/d \geq 2$  shedding of vortices with only one frequency are present in the flow; and biased flow with frequency modulation of the vortices shedding for the cases with  $L/d < 2$  are found. Also, Valencia *et al.* [7] numerically examined the unsteady turbulent flow field and heat transfer characteristics in a constant temperature-surfaced channel with stream wise periodically mounted square bars arranged side-by-side to the approaching flow. In that study, the effects of the transverse separation distance between the bars on the flow behavior and heat transfer were studied for a constant Reynolds number and periodicity length of the computational domain. The authors reported that the unsteady flow behavior, pressure drop and heat transfer are strongly dependent of the transverse separation distance of the bars.

On the other hand the unsteady, viscous flow past two bluff bodies such as cylinders or spheres has been the focus of numerous numerical and experimental investigations. Comprehensive archival correlations for average heat transfer coefficients for non-circular cylinders, circular cylinders and spheres in cross flow were reported by Sparrow *et al.* [8]. Their paper provided definitive information for surface-averaged Nusselt numbers for all text-book-standard bodies in cross-flow in air. The objects considered in their paper included cylinders whose cross-sections are square, diamond, and flat plate, perpendicular to the free stream, elliptical, hexagonal, rectangular, and circular. The characteristics of fluid flow and heat transfer across a long equilateral triangular cylinder placed in a horizontal channel was simulated by Srikanth *et al.* [9] for Reynolds number range 1-80 and Prandtl number of 0.71 for a fixed blockage ratio of 0.25.

In that study, the flow and temperature fields were presented by stream-line and isotherm profiles, respectively. In general, simple correlations for wake length, mean drag coefficient and average Nusselt number were obtained for the range of conditions studied here. The optimal parameters estimation for rectangular cylinders installed transversely in the flow channel of PEMFC from a three-dimensional PEMFC model and the Taguchi method was reported by Wu *et al.* [10]. The results indicated that the optimal combination factor is a cell temperature of 313K, an anode

humidification temperature of 333K, a cathode humidification temperature of 333K, a hydrogen stoichiometric flow ratio of 1.9, and an oxygen stoichiometric flow ratio of 2.7. This study also examined the pressure drop for the channels with rectangular cylinders transversely inserted. Huang *et al.*[11] a numerical study on the two-dimensional laminar mixed convective flow and heat transfer around two identical isothermal square cylinders arranged in tandem and confined in a channel by using the high accuracy multi domain pseudo spectral method. The spacing between the cylinders was fixed with four widths of the cylinder and the blockage ratio and the Prandtl number were fixed at 0.1 and 0.7 respectively.

The numerical results showed that, with the thermal buoyancy effect, the mixed convective flow sheds vortex behind the cylinders and keeps periodic oscillating. The variations of characteristic quantities related to flow and heat transfer processes, such as the overall drag and lift coefficients and the Nusselt numbers, were presented and discussed. A numerical analysis using Ansys Fluent was carried out by Kumar *et al.* [12] to investigate the forced convection of power-law fluids (power-law index varying from 0.2 to 1.8) around a heated semi-circular cylinder with wall confinement (or blockage ratio) of 25%, Prandtl number of 50, and Reynolds numbers 1-40. Their results were correlated in terms of wake length, drag coefficient and average Nusselt number expressions for various Reynolds numbers and power-law indices studied.

In addition, the effects of blockage ratios ranging from 16.67 % to 50 % on the engineering output parameters with varying power-law index at  $Re=40$  were reported. The flow characteristics and heat transfer performance of a rectangular channel with a small-scale circular cylinder vortex generator has recently been investigated numerically with Large Eddy Simulation (LES) by Wang *et al.* [13]. Their results showed that that the interaction between the cylinder wake and the wall boundary layer can dramatically alter the flow structure of the turbulent boundary layer.

Most of the previous investigations, cited above, on laminar and turbulent flows have focused on flow field and heat transfer characteristics for various bluff body height and spacing ratios for square bars, and non-circular, semi-circular, circular or shaped cylinders. The study on turbulent forced convection flows in a rectangular duct with flat bars detached from the walls has rarely been reported, especially for numerical work. In the present work, the numerical computations for two-dimensional turbulent forced convective flow and heat transfer around two detached identical adiabatic flat bars arranged in tandem and confined in a heated channel are conducted with the main aim being to examine the changes in the flow structure and heat transfer characteristics.

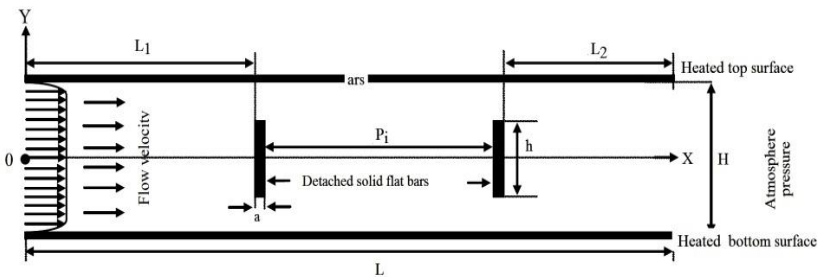


Fig. 1: Detail of the computational domain with the flat bars and boundary conditions. Flow is from left to right

2. MATHEMATICAL MODELING

2.1 Geometry of the present problem

In this simulation, the flow of air through a two-dimensional constant temperature-surfaced rectangular cross section channel, where two solid flat bars with the same cross-sectional areas were placed symmetrically in tandem along the channel axis, is studied. A schematic view of the physical problem with boundary conditions is shown in figure 1.

**Table 1** indicates the important geometry parameters of the computational domain. The fluid enters the channel at an inlet temperature,  $T_{in}$  and flows over a detached transverse bar pair mounted on the duct axis in tandem arrangement where  $h$  is the bar height,  $H$  set to 0.146 m, is the channel height and  $h/H$  is known as the blockage ratio,  $BR$ . The bar pitch-to-channel height ratio,  $P_i/H$  and the channel width-to-height aspect ratio,  $W/H$  are fixed at 0.97 and 1.32, respectively.

To investigate a geometry effect of the interaction between both the flat bars, the blockage ratio,  $h/H$  is varied in a range of  $BR = 0.16$  to  $0.50$  in the present investigation. The smooth rectangular channel was also checked out for a reference.

**Table 1:** Geometric details of the computation domain

Parameters of test channel en m	Values
Channel length, $L$	0.554
Channel length, $H$	0.146
Channel length, $W$	0.193
Hydraulic diameter, $D_h$	0.167
Flat bar thickness, $a$	0.01
Flat bar height, $h$	0.024 to 0.073
Flat bar distance or spacing, $P_i$	0.142
Distance upstream of the first bar, $L_1$	0.218
Distance downstream of the second bar, $L_2$	0.174

2.2 Flow governing equations

The numerical model for fluid flow and heat transfer in a rectangular channel was developed under the following assumptions:

- Steady two-dimensional fluid flow and heat transfer.
- The flow is turbulent and incompressible.
- Constant fluid properties.
- Body forces and viscous dissipation are ignored.
- Negligible radiation heat transfer.

Based on the above assumptions, the flow in rectangular channel is governed by the continuity, the Navier-Stokes and the energy equations. In the Cartesian tensor system these equations can be written as follows:

*Continuity equation*

$$\frac{\partial}{\partial x_j}(\rho u_j) = 0 \tag{1}$$

### Momentum equation

$$\rho u_j \frac{\partial u_i}{\partial x_j} = -\frac{\partial P}{\partial x_i} + \frac{\partial}{\partial x_j} \left( \mu \frac{\partial u_i}{\partial x_j} - \rho \overline{u_i u_j} \right) \quad (2)$$

### Energy equation

$$\frac{\partial}{\partial x_j} (\rho u_j T) = \frac{\partial}{\partial x_j} \left( (\Gamma + \Gamma_t) \frac{\partial T}{\partial x_j} \right) \quad (3)$$

where  $\Gamma$  and  $\Gamma_t$  are molecular thermal diffusivity and turbulent thermal diffusivity, respectively and are given by

$$\Gamma = \mu / \text{Pr} , \text{ and } \Gamma_t = \mu_t / \text{Pr}_t \quad (4)$$

The Reynolds-averaged approach to turbulence modeling requires that the Reynolds stresses,  $-\rho \overline{u_i u_j}$  in {Eq. (2)} needs to be modeled. For closure of the equations, the standard  $k-\varepsilon$  turbulence model (Launder *et al.*, [14]) is chosen. The classical approach is the use of Boussinesq hypothesis, relating Reynolds stresses and mean flow strain, through the eddy viscosity concept (Hinze [15]). In its general formulation, the Boussinesq hypothesis is written as,

$$-\rho \overline{u_i u_j} = \mu_t \left( \frac{\partial u_i}{\partial x_j} + \frac{\partial u_j}{\partial x_i} \right) - \frac{2}{3} \rho \delta_{ij} k \quad (5)$$

where  $\delta_{ij}$  represents the Kronecker delta,  $k$  is the turbulent kinetic energy, as defined by

$$k = \frac{1}{2} \overline{u_i u_i} \quad (6)$$

The turbulent viscosity term  $\mu_t$  is to be computed from an appropriate turbulence model. The expression for the turbulent viscosity is given as,

$$\mu_t = \rho C_\mu \frac{k^2}{\varepsilon} \quad (7)$$

The modeled equation of the TKE,  $k$  is written as,

$$\frac{\partial}{\partial x_i} (\rho k u_i) = \frac{\partial}{\partial x_j} \left( \left( \mu + \frac{\mu_t}{\sigma_k} \right) \frac{\partial k}{\partial x_j} \right) + G_k - \rho \varepsilon \quad (8)$$

Similarly the dissipation rate of TKE,  $\varepsilon$  is given by the following equation:

$$\frac{\partial}{\partial x_i} (\rho \varepsilon u_i) = \frac{\partial}{\partial x_j} \left( \left( \mu + \frac{\mu_t}{\sigma_\varepsilon} \right) \frac{\partial \varepsilon}{\partial x_j} \right) + C_{1\varepsilon} \frac{\varepsilon}{k} G_k - C_{2\varepsilon} \rho \frac{\varepsilon^2}{k} \quad (9)$$

In {Eqs. (8)} and {Eqs. (9)},  $G_k$  represents the production rate of the kinetic energy due to the energy transfer from the mean flow to turbulence, given by,

$$G_k = -\rho \overline{u_i u_i} \frac{\partial u_j}{\partial x_i} \quad (10)$$

The production term  $G_k$  is modeled according to Boussinesq's hypothesis, by,

$$G_k = \mu_t S^2 \tag{11}$$

where  $S$  is the modulus of the mean strain tensor, given by,

$$S = \sqrt{2S_{ij}S_{ij}} \tag{12}$$

and the strain tensor is:

$$S_{ij} = \frac{1}{2} \left( \frac{\partial u_i}{\partial x_j} + \frac{\partial u_j}{\partial x_i} \right) \tag{13}$$

This is the symmetrical part of the velocity gradient. The empirical constants in the turbulence transport equations are shown in **Table 2**.

**Table 2:** Empirical constant in the turbulent transport equations [14]

Constant	$C_\mu$	$C_{1\varepsilon}$	$C_{2\varepsilon}$	$\sigma_k$	$\sigma_\varepsilon$	$Pr_t$
Value	0.09	1.44	1.92	1.0	1.3	0.9

2.3 Boundary conditions

The solution domain of the considered two-dimensional flows is geometrically simple, which is a rectangle on the  $x-y$  plane, enclosed by the *inlet*, *outlet* and *wall* boundaries. The working fluid in this simulation is typically air and incompressible, which is taken as steady and in the turbulent state. The thermo-physical properties of air at 300K are listed in **Table 3**.

**Table 3:** The thermo-physical data of air at 300K [16]

Name	Air				
Material type	Fluid				
Fluent fluid materials	Air				
Property	Symbol	Unit	Value	Variation	
Density	$\rho$	kg/m <sup>3</sup>	1.225	Constant	
Specific heat at constant pressure	$C_p$	J/kg.K	1006.43	Constant	
Thermal conductivity	$\lambda_f$	W/m.K	0.0242	Constant	
Viscosity	$\mu$	kg/m.s	$1.7894 \times 10^{-5}$	Constant	
Prandtl number	$Pr$	-	0.71	Constant	

The computational domain and boundaries are presented in **Table 4**.

**Table 4:** Boundary conditions

$\phi=(u,v,k,\varepsilon,T)$	$u(m/s)$	$v(m/s)$	$k(m^2/s^2)$	$\varepsilon(m^2/s^3)$	$T(^{\circ}C)$
Inlet	$U_{in}$	0	$k_{in}=0.005U_{in}^2$	$\varepsilon_{in}=0.1k_{in}^2$	$T_{in}$
Outlet	$\frac{\partial u}{\partial x}=0$	$\frac{\partial v}{\partial x}=0$	$\frac{\partial k}{\partial x}=0$	$\frac{\partial \varepsilon}{\partial x}=0$	$\frac{\partial T}{\partial x}=0$
Walls	0	0	0	0	$T_w$

The temperature of the working fluid,  $T_{in}$  is set equal to  $27^{\circ}\text{C}$  (300K) at the inlet of the channel ( $x=0$ ,  $-H/2 \leq y \leq H/2$ ). A uniform one-dimensional velocity profile,  $U_{in}$  is applied as the hydraulic boundary condition at the inlet of the computational domain, as shown in figure 1 and **Table 4**. The turbulence intensity was kept at  $I=2\%$  at the inlet. The pressure at the inlet of the computational domain was set equal to the zero gauge.

Aluminum is selected as the solid material, and the parameters are given in **Table 5**.

**Table 5:** Thermo-physical data of aluminium at 300 K [16]

Name			Air	
Chemical formula			Al	
Material type			Solid	
Fluent fluid materials			Aluminium	
Property	Symbol	Unit	Value	Variation
Density	$\rho$	$\text{kg/m}^3$	2719	Constant
Specific heat at constant pressure	$C_p$	$\text{J/kg.K}$	871	Constant
Thermal conductivity	$\lambda_s$	$\text{W/m.K}$	202.4	Constant

The constant temperature of the bottom and upper walls is maintained at  $T_w=102^{\circ}\text{C}$ , (375K) while the bars are assumed at adiabatic wall conditions. At the solid/fluid interface, the following conditions are applied:

*Heat flux continuity*

$$\lambda_f \left. \frac{\partial T_f}{\partial x} \right|_{\tilde{N}} = \lambda_s \left. \frac{\partial T_s}{\partial x} \right|_{\tilde{N}} \quad (14)$$

*Temperature continuity*

$$T_f|_{\tilde{N}} = T_s|_{\tilde{N}} \quad (15)$$

Where  $\tilde{N}$  is the normal coordinate to the wall.

Besides, no-slip and impermeability boundary conditions are imposed at the channel walls as well as the bar surfaces. In the channel outlet, all gradients are set to zero and the pressure is the atmospheric pressure  $P_{atm}$  (**Table 4**).

The Reynolds number based on the channel hydraulic diameter,

$$D_h = \frac{2HW}{(H+W)} \quad (16)$$

is given by,

$$Re = \frac{\rho U D_h}{\mu} \quad (17)$$

where  $\rho$  is the fluid density,  $\mu$  is the fluid viscosity, and  $\bar{U}$  is the channel average velocity.



The heat transfer is measured by local Nusselt number,  $Nu_x$  which can be written as,

$$Nu_x = \frac{h_x D_h}{\lambda_f} \quad (18)$$

where  $\lambda_f$  is the thermal conductivity of the fluid, and  $h_x$  is the local convective heat transfer coefficient.

The average Nusselt number,  $\overline{Nu}$  is the arithmetic average of all local Nusselt numbers along the heated part of the channel, which can be obtained by,

$$\overline{Nu} = \frac{1}{L} \int Nu_x \partial x \quad (19)$$

The skin friction coefficient,  $C_f$  is given by,

$$C_f = \frac{\tau_w}{1/2 \rho \overline{U}^2} \quad (20)$$

The friction factor,  $f$  is evaluated from the pressure drop as,

$$f = \frac{(\Delta P/L) D_h}{1/2 \rho \overline{U}^2} \quad (21)$$

where  $\tau_w$  represents the wall shear stress,  $\Delta P$  the pressure drop across the heated test section and  $L$  is the length of the heated test section.

### 3. NUMERICAL METHOD

The Commercial CFD software Fluent 6.3 [16] was used to simulate the fluid flow field and heat transfer characteristics. As a part of the same package, a preprocessor Gambit 2.3 was used to generate the required mesh for the solver. The time-independent incompressible Navier-Stokes equations and the turbulence model were discretized using the Finite Volume Method, details of which can be found in Patankar [17]. For closure of the equations, the standard  $k-\epsilon$  model based on Launder *et al.* [14] was used in the present study. The convection terms in the equations were approximated using a Power-Law scheme.

The method uses staggered grids and Cartesian velocity components, handles the pressure-velocity coupling with the Simplec-algorithm in the form given by Van Doormaal *et al.* [18] and solves the resulting system of equations iteratively with a Tri-Diagonal-Matrix algorithm. The solutions were converged when the normalized residual values were less than  $10^{-6}$  for all variables,  $\phi \equiv (u, v, k, \epsilon)$  but less than  $10^{-9}$  only for the energy equation,  $\phi \equiv (T)$ .

#### 3.1 Grid independent

The mesh was generated by the pre-processor software Gambit 2.3 [16]. The mesh of the computational model is shown in figure 2. The mesh was refined at all solid boundaries. This refinement was necessary to resolve the strong velocity and temperature gradients in that region. For the regions more distant from the walls, the mesh is uniform.

Structured meshes, with quadrilateral elements were built and tested with the Fluent 6.3 [16]. To check grid independence in this computation, the case with symmetrically mounted arrays of detached flat bars in the rectangular channel was

simulated with the standard  $k-\epsilon$  model [14] for three different grid densities of (175×55) cells, (215×85) cells, and (255×115) cells with  $W/H=1.32$ ,  $P_i/H=0.97$ , and  $a=0.01\text{m}$ . The results of the grids independent test are shown in **Table 6**.

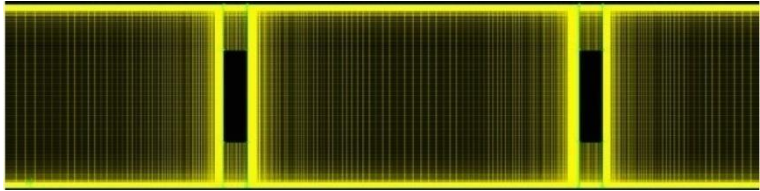


Fig. 2: The Mesh of a computational domain section with two detached flat bars in tandem arrangement,  $BR = 0.50$

The calculation with the different grids were performed from the test values of the average Nusselt numbers with different bar sizes ( $BR=0.16$ , and  $0.50$ ) and for various values of Reynolds number ( $Re=10000$ , and  $25.000$ ).

In the table, it is visible that the variation in  $\overline{Nu}$  at the heated top surface ( $y=H/2$ ) between the three resolutions over a sufficiently large range of  $Re$  is small ( $< 2\%$ ).

**Table 6:** Averaged values of Nusselt number at ( $0 \leq x \leq L$ ,  $y=H/2$ ) for different grid sizes in the case of  $W/H=1.32$ ,  $P_i/H=0.97$ , and  $a=0.01\text{m}$

Case	Re	Average Nusselt number ( $\overline{Nu}$ )		
		(175×55) cells	(215×85) cells	(255×115) cells
BR=0.16	10.000	267.8109 (1.08%)	264.9495 (0%)	264.9495
	25.000	517.4587 (1.62%)	513.6906 (0.88%)	509.2096
BR=0.50	10.000	276.3242 (1.78%)	271.4917 (0%)	271.4917
	25.000	528.3471 (1.69%)	525.6454 (1.17%)	519.5665

The number within brackets gives the percentage deviation relative to the (255×115) cells. The above tests show that adequately resolved results can be obtained on a grid system of (175×55) cells for  $Re=10000$  and a grid system of (215×85) cells for  $Re=25000$ . With the mentioned grids, spatial resolution is small enough to allow reasonable computation time, and as seen previously, good enough to provide accurate data.

3.2 Verification of smooth channel

The current numerical data on heat transfer and friction factor characteristics in a  $W/H=1.32$  smooth channel with constant wall temperature are first validated in terms of average Nusselt number,  $\overline{Nu}_0$  and friction factor,  $f_0$ . The results of  $\overline{Nu}_0$  and  $f_0$  obtained from the present smooth channel without bars are compared with those from the steady state flow correlations of Dittus-Boelter *et al.* from Incropera and Dewitt [19] for turbulent flow in ducts.

Nusselt number correlation from Dittus-Boelteris of the following form for  $Re \geq 10000$ , heating,

$$\overline{Nu}_0 = 0.023 Re^{0.8} Pr^{0.4} \tag{22}$$

The friction factor correlation from Petukhov is of the form,

f\_0 = (0.79 ln Re - 1.64)^-2 (23)

Petukhov equation is valid for 3000 ≤ Re ≤ 5×10<sup>6</sup>.

Table 7 shows a comparison of Nu<sub>0</sub> and f<sub>0</sub> obtained from the present numerical simulation using the standard k-ε turbulence model [14] with those from correlations [19] of {Eqs. (22)} and {Eqs. (23)}. In the table, the present numerical smooth duct result is found to be in excellent agreement with correlation solutions obtained from the open literature [19] for both the Nusselt number and the friction factor with in ±0.12% and ±1.00% maximum deviations, respectively. These results give confidence that the numerical method used was accurate.

Table 7: Verification of smooth channel

Re	Exact solution [19]		Present numerical study		Error (%)	
	Nu <sub>0</sub>	f <sub>0</sub>	Nu <sub>0</sub>	f <sub>0</sub>	Nu <sub>0</sub>	f <sub>0</sub>
10000	31.7856	0.0314	31.8221	0.0311	0.1150	-0.7524
12500	37.9978	0.0295	38.0412	0.0296	0.1144	0.5745
15000	43.9647	0.0281	44.0135	0.0282	0.1112	0.6911
17500	49.7349	0.0270	49.7914	0.0272	0.1138	0.9037
20000	55.3420	0.0261	55.4042	0.0262	0.1125	0.5500
22500	60.8103	0.0253	60.8821	0.0254	0.1181	0.7478
25000	66.1581	0.0247	66.0804	0.0246	-0.1173	-0.5603

3.3 Effect of turbulence models

To ensure realistic and accurate turbulent modeling, the performance of four different turbulence models, namely Standard k-ε model [14], Low Reynolds Number (LRN) k-ε model [20, 21], Standard k-ω model [22], and Shear Stress Transport (SST) k-ω model [23] are evaluated by solving Navier-Stokes equations. The predicted results are reported for two-dimensional incompressible flow of air through the W/H=1.32 smooth channel with the constant wall temperature condition along the top and bottom walls at Reynolds number, Re = 10000 based on the entrance velocity, U<sub>in</sub> = 0.9 m/s .

Table 8 compares the average top surface Nusselt number (Nu<sub>0</sub>) of the smooth channel bars predicted by the above simulations with the exact solution values obtained from the correlation of {Eq. (22)} under a similar operating condition.

Table 8: Effect of turbulence models on Nu<sub>0</sub> at the heated top surface (0 ≤ x ≤ L, y=H/2) in the smooth wall channel without bars for Re = 10000

Turbulence model	Nu <sub>0</sub>	Relative error (%)
Standard k-ε [14]	31.8221	0.1148
LRN k-ε [20, 21]	35.6157	0.1204
Standard k-ω [22]	41.3498	0.3009
SST k-ω [23]	40.0371	0.2596
Correlation of Dittus-Boelter	31.7856	(Reference calculations)

The table shows the percent error, δ defined as,

$$\delta = \left| \frac{\overline{Nu}_{ref} - \overline{Nu}}{\overline{Nu}_{ref}} \right| \tag{23}$$

The numerical predicted result with the standard  $k-\varepsilon$  turbulence model or the LRN  $k-\varepsilon$  model agrees well with the Nusselt number correlation data of Dittus-Boelter than that with the standard  $k-\omega$  model or the SST  $k-\omega$  model. The predicted and measured results are in a similar trend for using both the standard  $k-\varepsilon$  model and the LRN  $k-\varepsilon$  model. Thus, any of the standard  $k-\varepsilon$  model or the LRN  $k-\varepsilon$  model appears to be suitable in prediction of this flow. Considering both convergent time and solution precision, the standard  $k-\varepsilon$  turbulence model was selected to use in prediction of this complex flow.

4. RESULTS AND DISCUSSION

4.1 Effect of flow Reynolds number ( Re )

Flat bars play an important role in the dynamics of the airflow through shell-and-tube heat exchangers. For the better comprehension of the phenomena produced by these devices, the search of detailed information's about the fluid flow characteristics is necessary. In this work, the forced convective incompressible flow through a constant temperature-surfaced rectangular cross section channel, where two adiabatic flat bars with the same cross-sectional areas were placed symmetrically in tandem arrangement, is studied.

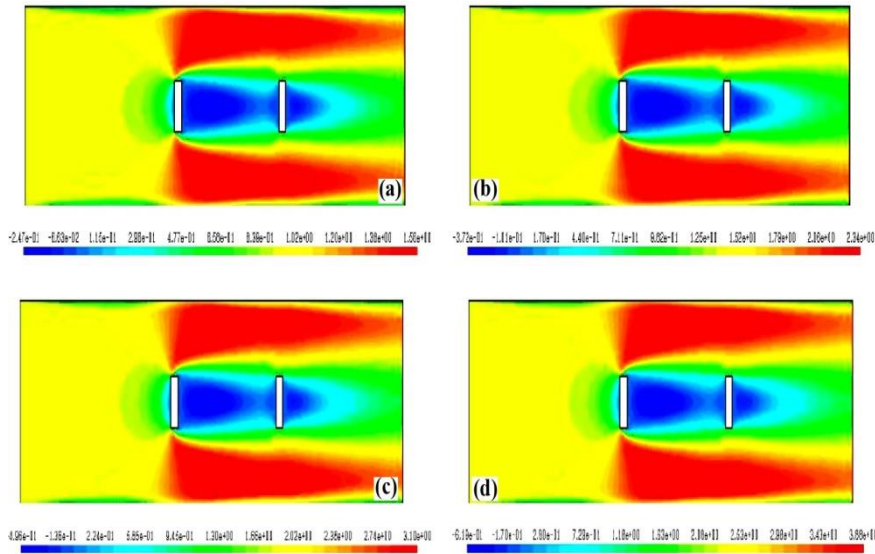


Fig. 3: Variation of axial velocity fields with Reynolds number for BR = 0.25  
(a) Re = 1000 , (b) Re = 15000 , (c) Re = 20000 , (d) Re = 25000  
Flow is from left to right. Velocity values in m/s

The airflow structure in the presence of a flat bar pair could be easily discerned by considering the contour plots of axial velocity fields as depicted in figure 3-a, -b,

**-c** and **-d** for the cases of  $Re=1000$ ,  $15000$ ,  $20000$  and  $25000$ , respectively. Here the axial velocity fields around the adiabatic tandem flat bar module are presented using the  $k-\varepsilon$  standard at  $W/H=1.32$ ,  $P_i/H=0.97$ , and  $a=0.01\text{m}$ .

For all Reynolds numbers used in this Section (4.1), the bar height-to-channel height ratio ( $h/H$ ) or blockage ratio ( $BR$ ) was kept constant at  $BR=0.25$ . This corresponds to the area reduction of 25% at the transverse bars. In the figure, the result analyses show very low velocity values adjacent to the flat bars.

In the regions downstream of both flat bars, recirculation cells/vortices with very low velocity values are observed. In the regions between the tip of the flat bars and the top and bottom channel walls, the velocity is increased. Due to the changes in the flow direction produced by the transverse bars, the highest velocity values appear near the channel walls with an acceleration process that starts just after the first flat bar. The comparison of results in figure 3-a to -d indicates that the airflow rate in terms of Reynolds numbers has an impact on the axial velocity field contours.

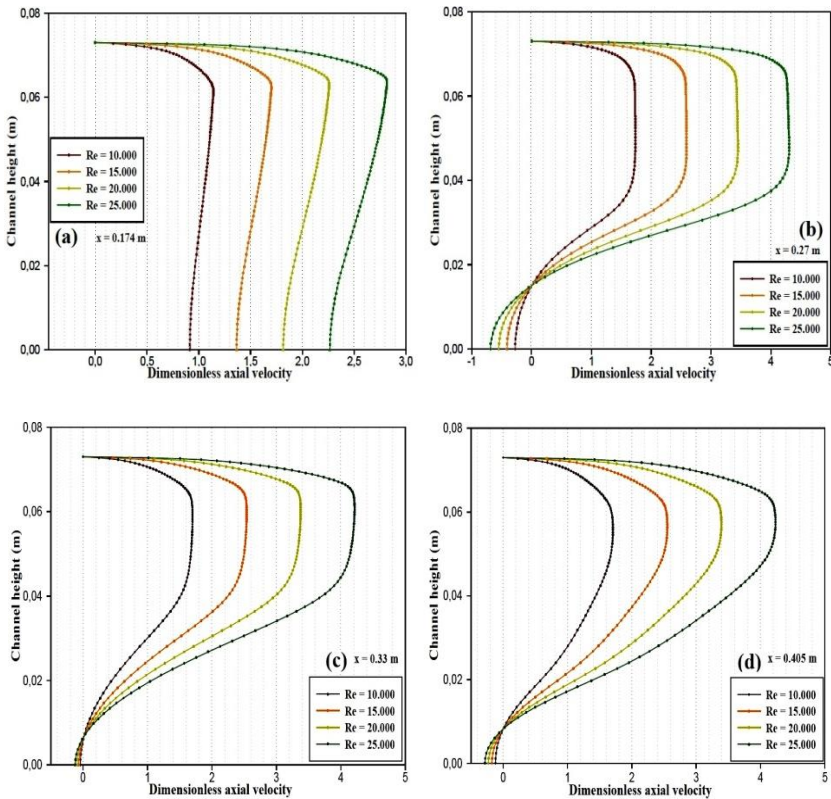


Fig. 4: Dimensionless axial velocity profiles as a function of Reynolds number in the upper half of the channel for  $BR=0.25$  at different transverse locations:

- (a) 0.044 m upstream of the first flat bar at  $x=0.174\text{ m}$ , (b) between the first and the second flat bars at  $x=0.270\text{ m}$ , (c) 0.04 m upstream of the second flat bar at  $x=0.330\text{ m}$ , (d) 0.025 m after the second flat bar at  $x=0.405\text{ m}$ .

Figure 4-a to -d presents the dimensionless axial velocity profile results (the velocity values are scaled to the velocity at the entrance, which is  $U_{in} = 0.9 \text{ m/s}$ ) for air flow in the upper half of the symmetric channel for four different axial stations  $x = 0.174, 0.270, 0.330$ , and  $0.405 \text{ m}$ , measured from the upstream end of the test channel, respectively. In the figure, the dimensionless axial velocity profiles are related as a function of Reynolds number ( $10000 \leq Re \leq 25000$ ) at  $W/H=1.32$ ,  $P_i/H=0.97$ ,  $BR=0.25$  and  $a=0.01 \text{ m}$ .

The comparison of dimensionless axial velocity profiles at different Reynolds numbers shows that the airflow is accelerated and redirected near the flat bars. The influence of the deformation of the flow field increases as the flow approaches the first bar, increasing the velocity of the flow approaching the passage above the bar, as shown in figure 4-a, at position given by  $x = 0.174 \text{ m}$ ,  $0.044 \text{ m}$  before the first flat bar. Downstream, at location  $x = 0.270 \text{ m}$  from entrance,  $0.042 \text{ m}$  after the first flat bar, as a result of sudden expansion in the cross-section, the flow separates, a larger clockwise vortex is formed behind the first bar and flow reattachment is then established, as presented in figure 4-b. A similar phenomenon is observed near the second flat bar placed symmetrically on the channel axis with counterclockwise vortices at the upstream and downstream bar, as illustrated in figure 4-c and -d, respectively.

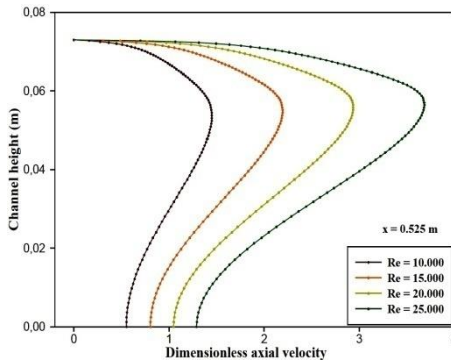


Fig. 5: Dimensionless axial velocity profiles as a function of Reynolds number in the upper half of the channel after the second flat bar, near the channel outlet,  $BR = 0.25$

A comparison of numerical results of dimensionless axial velocity profiles after the second flat bar, near the channel outlet is presented in figure 5. At a position  $x = 0.525 \text{ m}$ ,  $0.029 \text{ m}$  before channel outlet, the value of the velocity reaches  $1.3059 - 3.3174 \text{ m/s}$ ,  $1.451 - 3.686$  times higher than the entrance velocity, depending on the  $Re$  values. These values are only possible due to the very strong flow recirculation on the back side of the first flat bar, which leads air from outside of the channel into the computational domain. Concerning the effect of the Reynolds number on the airflow characteristics, it can be seen from these figures 4 and 5 and for this blockage ratio ( $BR = 0.25$ ), that the axial velocity value tends to increase with the rise of Reynolds number values for all locations. By increasing the Reynolds number  $Re$ , the flow reattaches on the bar surfaces and downstream, while recirculation lengths are increased.



The axial variation of the Nusselt number,  $Nu_x$  for the heated top surface ( $0 \leq x \leq L$ ,  $y = H/2$ ) with various Reynolds number values at  $W/H=1.32$ ,  $P_i/H=0.97$ ,  $BR=0.25$  and  $a=0.01m$  is presented in figure 6. These profiles present in all cases a minimum and a maximum of the heat transfer rate. In the figure, the trends of  $Nu_x$  are similar for all  $Re$  values. As expected, the largest variations are found near the tip of the bars, due to the strong velocity gradients in that region. The  $Nu_x$  values tend to drop considerably to almost zero when it reaches the first bar. Downstream, the  $Nu_x$  increase gradually until reaching the area of the second bar where the maximum  $Nu_x$  value occurs and then shows an abrupt reduction through the exit. Concerning the effect of the Reynolds number on the heat transfer characteristics, it can be seen from this figure that values of local Nusselt number become higher with increasing values in flow Reynolds number, because when the  $Re$  increases, the turbulence increases and the recirculation region.

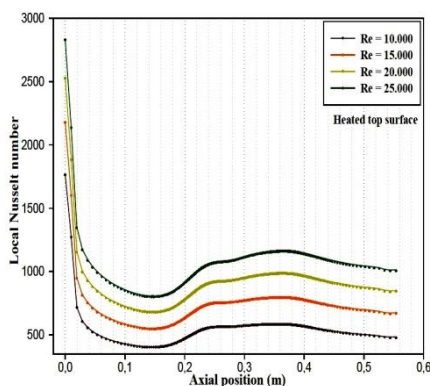


Fig. 6: Local Nusselt number versus Reynolds number,  $BR = 0.25$

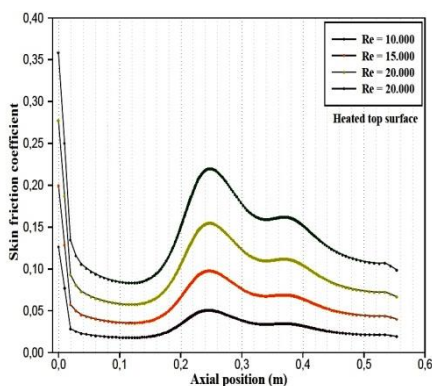


Fig. 7: Skin friction coefficient versus Reynolds number,  $BR = 0.25$

In general, the augmentation in heat transfer is concerned with penalty in terms of increased skin friction coefficient leading to higher pressure drop. Figure 7 shows the skin friction coefficient,  $C_f$  along the upper channel wall ( $0 \leq x \leq L$ ,  $y = H/2$ ) for different Reynolds number values ( $Re=10000$ ,  $15000$ ,  $20000$  and  $25000$ ) in the cases of  $W/H=1.32$ ,  $P_i/H=0.97$ ,  $BR=0.25$  (constant) and  $a=0.01m$ . In the figure, it is evident that the presence of flat bars involves the increased value of surface friction on the channel walls. Similarly to the results in figure 6, the greatest  $C_f$  values are found near the tip of the bars, due to the strong velocity gradients in that region.

In the figure, the increase of skin friction coefficients is found to be larger than that of the heat transfer coefficients caused by the temperature field. This may imply that the flow field develops more rapidly than the temperature field. The peak skin friction coefficient ( $C_f$ ) can be observed in the region opposite the bars at the locations corresponding to the zones of recirculation (Figures 4-b, 4-d, and 7) while the lowest of the skin friction coefficient is found in the region upstream of the first bar due to the low velocities in that region and at the exit for all  $Re$  values.

The latter is caused by the absence of the bars. The influence of flow Reynolds number on the skin friction is also presented in figure 7. The trends of  $C_f$  are similar for all Re values. In the figure, it is worth noting that the skin friction coefficient tends to increase with the rise of Reynolds number for all locations.

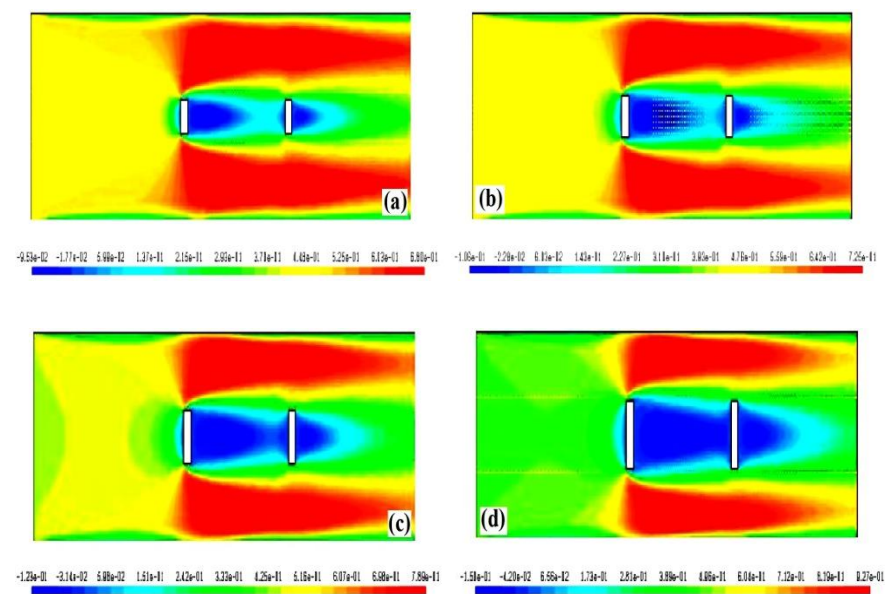
**4.2 Effect of blockage ratio ( BR )**

The impact of the flat bar height on the heat transfer and fluid flow characteristics was investigated for five different blockage ratios ( BR ), which were 0.16, 0.20, 0.25, 0.33, and 0.5 m. This corresponds to the flow area reduction of 16, 20, 25, 33, and 50 %, at the flat bars.

The distance between the flat bars or spacing ( $P_1$ ) was kept constant at 0.142 m. The numerical results on the structure of the near wall flow in a channel with two tandem flat bars are presented in the range of blockage ratios ( $0.16 \leq BR \leq 0.5$ ) for fixed values of other parameters ( $W/H=1.32$ ,  $P_1/H=0.97$ ,  $a=0.01m$ , and  $Re=10000$ ) in the form of fields of axial velocity as displayed in figure 8.

These results give a good visualization of the flow evolution around the flat bars. Low and high velocity regions are associated to recirculation regions. The most intense is that occurring downstream of the first flat bar, responsible for the high flow velocities observed at the outlet of the computational domain, creating a negative velocity which introduces mass inside the test channel through the outlet.

The plot also shows that the bar height has a significant impact on the vortex size downstream of the bars. The size of the recirculation zone behind the first bar is found to be larger than the ones at the corner and its height is approximately equal to the extent of the flow blockage by the bar, which is equal to  $h=0.02336$ ,  $0.0292$ ,  $0.0365$ ,  $0.04818$ , and  $0.073$  m for the cases shown respectively in figure 8-a to -e, depending on the BR values.





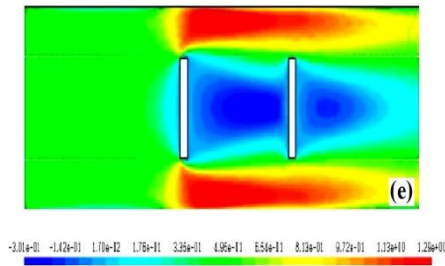


Fig. 8: Variation of axial velocity fields with blockage ratio for  $Re=10000$   
(a)  $BR = 0.16$ , (b)  $BR = 0.20$ , (c)  $BR = 0.25$ , (d)  $BR = 0.33$ , and (e)  $BR = 0.55$   
Airflow is from left to right. Velocity values in m/s

The vortex length is also influenced by the height of the flat bars. In the figure, the vortex length for air flowing in the channel with larger blockage ratio is found to be higher than that with smaller blockage ratio. The vortex length increase with  $BR$  up to  $BR = 0.5$ . The larger bar height, the longer the re-circulation zone becomes.

The variation of channel flow velocity appears clearly on the contours and their scales which present positive and negative values. In order to better analyze this evolution, we plotted dimensionless axial velocity curves in the upper half of the symmetric channel at these transverse locations:  $x = 0.270$ ,  $0.405$ , and  $0.525$  m, as presented in figures 9-a, -b, and -c, respectively.

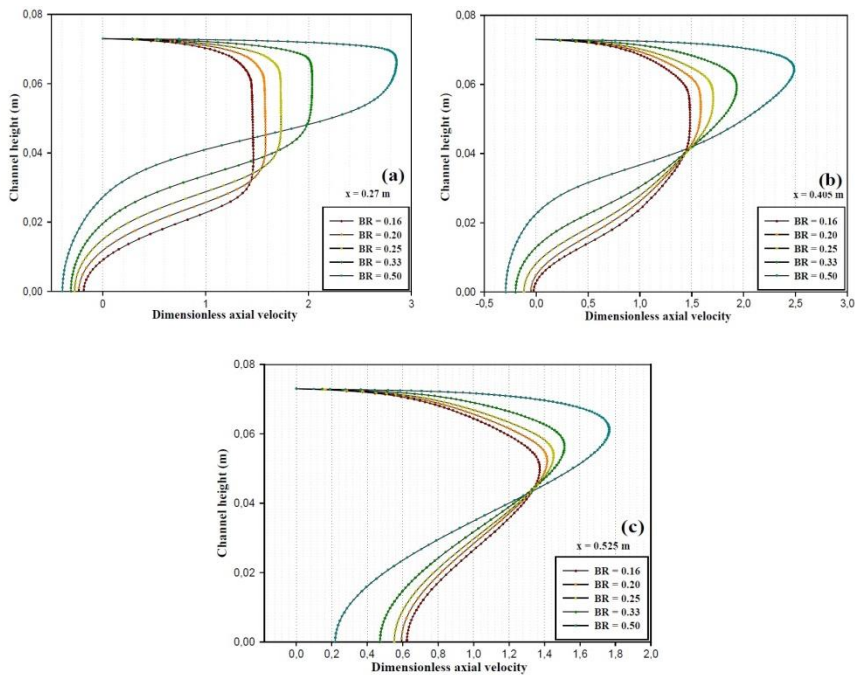


Fig. 9: Variation of dimensionless axial velocity profiles with  $BR$  in the upper half of the channel for stations: (a) between the first and the second flat bars at  $x = 0.270$  m, (b) at  $x = 0.405$  m, and (c) at  $x = 0.525$  m.

(b) downstream of the second flat bar at  $x = 0.405\text{ m}$ , (c) near the channel outlet at  $x = 0.525\text{ m}$ ,  $\text{Re}=10000$

Between the flat bars, at locations  $x = 0.270\text{ m}$  from entrance,  $0.042\text{ m}$  after the first flat bar, the flow is characterized by very high velocities at the upper part of the upper half of the channel. The increases in velocity values for using  $\text{BR}=0.16$ ,  $0.20$ ,  $0.25$ ,  $0.33$ , and  $0.50$ , reach respectively  $1.463$ ,  $1.583$ ,  $1.733$ ,  $2.035$ , and  $2.855$  times higher than the entrance velocity, which is  $U_{\text{in}} = 0.9\text{ m/s}$ , as shown in figure 9-a.

In the lower part, negative velocities indicate the presence of vortex behind the first flat bar. The numerical results of dimensionless axial velocity distributions at a position  $x = 0.405\text{ m}$ ,  $0.025\text{ m}$  after the second flat bar, are shown in figure 9-b. Similarly to the results in figure 9-a, the largest variations are found near the upper wall of the channel ( $0 \leq x \leq L$ ,  $y = H/2$ ), due to the strong velocity gradients in that region.

In the region downstream of the considered flat bar, where there circulation is strongly influenced by the height of the bar, increasing when bar length is increased. Near the channel outlet at the position  $x = 0.525\text{ m}$  from entrance, as presented by figure 9-c, the flow is characterized by very high velocities at the upper part of the channel, near the heated top surface with an acceleration process that starts just after the first flat bar (see figure 8).

Downstream of the second flat bar at the distance equal to  $0.029$  before the channel exit, dimensionless axial velocity profiles present low values, meaning that the pressure in that location is below atmospheric pressure ( $P_{\text{atm}}$ ). This fact is associated to the negative velocities in the regions downstream of both flat bars (see figure 9-a and -b). The flow pattern is also affected by the flat bar height as it appears in figure 9. Increasing  $\text{BR}$ , when  $\text{Re}$  is kept at a constant value ( $\text{Re}=10000$ ), leads to a disruption of the flow and the formation of a vortex behind each flat bars.

In addition, the flow velocity for air flowing in the flat-bar channel with larger blockage ratio is found to be higher than that with smaller blockage ratio. The velocity increases with the increase of blockage ratio,  $\text{BR} (h/H)$  and thus, the  $\text{BR} = 0.25$  provides maximum axial velocity for all locations.

The numerical results on heat transfer and flow friction characteristics in a two-dimensional isothermal-wall rectangular channel fitted with two flat bars of five heights,  $h=0.02336$ ,  $0.0292$ ,  $0.0365$ ,  $0.04818$ , and  $0.073\text{ m}$  ( $h/H$  or  $\text{BR} = 0.16$ ,  $0.20$ ,  $0.25$ ,  $0.33$  and  $0.50$ ), are presented in the form of  $\overline{\text{Nu}}$  and  $f/f_0$  as displayed in figures 10 and 11, respectively.

In figure 10, it is found that the average Nusselt number increases with increasing the  $\text{BR}$ , apart from the  $\text{Re}$  values. The higher  $\overline{\text{Nu}}$  can be seen at the larger  $\text{BR}$ . This is because the larger bar height causes flow separation and provides better increase in the turbulence intensity of the flow than the lower one. The peak value of  $\overline{\text{Nu}}$  from using the bars is found to be about  $7835 - 12505$  times over the channel with no bar, depending on the  $\text{BR}$  and Reynolds number values.

This indicates a merit of employing the bar over the smooth channel for enhanced heat transfer. For using the bars, the  $\overline{Nu}$  with larger blockage ratio is found to be higher than that with smaller blockage ratio. The average Nusselt number increases with the increase of blockage ratio ( BR ) and thus, the  $BR = 0.50$  provides maximum Nusselt number.

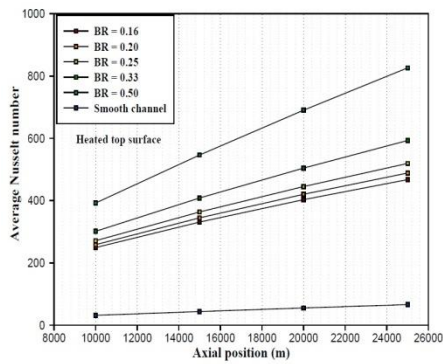


Fig. 10: Variation of  $\overline{Nu}$  with Reynolds number for various bar BRs

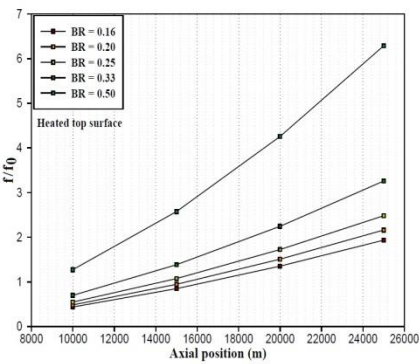


Fig. 11: Variation of  $f/f_0$  with Reynolds number for bars at various BRs

In figure 11, it is worth noting that the friction factor ratio value,  $f/f_0$  tends to increase with the rise of Reynolds number for all flat bar height cases. The use of the bar leads to extremely considerable increase in friction factor in comparison with the plain channel with no bar. This can be attributed to the flow blockage, higher surface area and the act caused by the reverse flow due to the presence of rectangular-bars.

For using the bars, the increase in the blockage ratio value gives rise to the augmentation of friction factor. The mean increase in the friction factor ratio of using the flat bar is in a range of 0.439 to 7.945 times over the smooth channel, depending on the BR and Reynolds number values. The  $f/f_0$  value of the bar at  $Re=10000 - 25000$  and  $BR = 0.50$  is found to be around 1821 - 1928, 2321 - 2531, 2620 - 2905, and 2899 - 3248 times higher than that with  $BR = 0.33, 0.25, 0.20,$  and  $0.16,$  respectively. The losses mainly are due to high viscous losses near the wall, to the extra forces exerted by reverse flow and to the high flow blockage from the presence of the flat bars.

### 5. CONCLUSION

The research work has been conducted to assess turbulent forced convection heat transfer and friction loss behaviors for a two-dimensional incompressible flow of a Newtonian fluid through a constant temperature-surfaced rectangular cross section channel, containing two detached flat bars with the same cross-sectional areas in a tandem arrangement. To investigate turbulence model effects, computations based on a Finite Volume approach, have been carried out by utilizing four turbulence models: the Standard  $k-\varepsilon$ , the Low Reynolds Number (LRN)  $k-\varepsilon$ , the Standard  $k-\omega$ , and the Shear Stress Transport (SST)  $k-\omega$  turbulence models.

Measurements have been carried out for the channel of aspect ratio,  $AR=1.32$  and hydraulic diameter,  $D_h = 0.167\text{m}$  with five different bar blockage ratios, ( $BR = 0.16, 0.20, 0.25, 0.33$  and  $0.50$ ) while the bar pitch spacing ratio is set to  $0.97$  and kept constant. Air was the working fluid with the flow rate in terms of Reynolds numbers ranging from  $10000$  to  $25000$ .

The predicted results from using several turbulence models reveal that the Standard and LRN  $k-\varepsilon$  turbulence models generally provide better agreement with measurements than others. Therefore, the  $k-\varepsilon$  model was selected to use in prediction of this complex flow.

In addition, the results of the steady flow behavior, convective heat transfer and pressure drop were also examined. Large recirculation regions and velocity gradients were observed behind the tandem transverse bars. In general, Nusselt number and friction loss increase with the rise in blockage ratio values for all Reynolds numbers used.

### AUTHOR'S CONTRIBUTIONS

Each author of this manuscript made considerable contributions in developing the mathematical modeling, data-analysis and contributed to the writing of this manuscript.

### NOMENCLATURE

$a$	Flat bar thickness, m	$u$	Fluid velocity in the $x$ -direction, m/s
$BR$	Blockage ratio	$u_i$	Mean velocity component in the
$C_p$	Specific heat at constant pressure, J/kg.K	$u_j$	$x_i$ -, $x_j$ -direction, m/s
$C_f$	Skin friction coefficient	$u'_i$	Fluctuation velocity components
$C_{1\varepsilon}$	Constant used in the standard $k-\varepsilon$ model	$u'_j$	in $x_i$ -, $x_j$ - direction, m/s
$C_{2\varepsilon}$	Constant used in the standard $k-\varepsilon$ model	$v$	Fluid velocity in the $y$ -direction, m/s
$C_\mu$	Constant used in the standard $k-\varepsilon$ model	$W$	Channel width, m
$D_h$	Hydraulic diameter of rectangular channel, m	$x, y$	Cartesian coordinates, m
$f$	Friction factor	$\varepsilon$	Specific dissipation rate, $\text{m}^2/\text{s}$
$G_k$	Production of turbulent kinetic energy, $\text{m}^2/\text{s}^2$	$\Gamma$	Molecular thermal-diffusivity, $\text{kg}/\text{m.s}$
$H$	Channel height, m	$\Gamma_t$	Turbulent thermal-diffusivity, $\text{kg}/\text{m.s}$
$h$	Flat bar height, m	$\delta_{ij}$	Kronecker delta
$h_x$	Local convective heat transfer coefficient, $\text{Wm}^{-2}\text{K}^{-1}$	$\rho$	Fluid density, $\text{kg}/\text{m}^3$
$k$	Turbulent kinetic energy, $\text{m}^2/\text{s}^2$	$\lambda_f$	Fluid thermal conductivity, $\text{W}/\text{m}^\circ\text{C}$
$L$	Length of rectangular channel in $x$ -direction, m	$\lambda_s$	Solid thermal conductivity, $\text{W}/\text{m}^\circ\text{C}$
$L_1$	Distance upstream of the first flat bar, m	$\mu$	Molecular viscosity, $\text{kg}/\text{m.s}$
$L_2$	Distance downstream of the second flat bar, m	$\mu_t$	Eddy viscosity, $\text{kg}/\text{m.s}$
$\bar{N}$	Coordinate normal to the wall	$\sigma_k$	Turbulent Prandtl number for $k$ -equation
$\bar{Nu}$	Average Nusselt number	$\sigma_\varepsilon$	Turbulent Prandtl number for $\varepsilon$ -equation
$Nu_x$	Local Nusselt number	$\tau_w$	Wall shear stress, $\text{kg}/\text{s}^2\text{m}$
$\Delta P$	Pressure drop, Pa	$\phi$	Stands for the dependent variables $u, v, k, \varepsilon$ and $T$
$P$	Pressure, Pa	$\delta$	Prescribed error
$P_{atm}$	Atmospheric pressure, Pa	$atm$	Atmospheric
$P_i$	Flat bar distance or spacing, m	$f$	Fluid
$Pr$	Prandtl number	$i, j$	Refers coordinate direction vectors
$Pr_t$	Turbulent Prandtl number	$in$	Inlet of the computational domain
$Re$	Reynolds number	$s$	Solid
$S$	Modulus of the mean rate-of- strain tensor	$t$	Turbulent
$S_{ii}$	Strain tensor	$w$	Wall
$T$	Temperature, $^\circ\text{C}$	$x$	Local
$T_{in}$	Inlet temperature, $^\circ\text{C}$	$U_{in}$	Inlet velocity, m/s
$T_w$	Wall temperature, $^\circ\text{C}$		
$\bar{U}$	Mean axial velocity of the section, m/s		

## REFERENCES

- [1] T.-M. Liou, W.-B. Wang and Y.-J. Chang, '*Holographic Interferometry Study of Spatially Periodic Heat Transfer in a Channel with Ribs Detached From One Wall*', Journal of Heat Transfer, Vol. 117, N°1, pp. 32 - 39, 1995.
- [2] T.-M. Liou and S.-H. Chen, '*Turbulent Heat and Fluid Flow in a Passage Disturbed by Detached Perforated Ribs of Different Heights*', International Journal of Heat and Mass Transfer, Vol. 41, Issue 12, pp. 1795 - 1806, 1998.
- [3] J.P. Tsia and J.J. Hwang, '*Measurements of Heat Transfer and Fluid Flow in a Rectangular Duct with Alternate Attached–Detached Rib-Arrays*', International Journal of Heat and Mass Transfer, Vol. 42, Issue 11, pp. 2071 - 2083, 1999.
- [4] J. Alvarez, M. Pap and A. Valencia, '*Turbulent Heat Transfer in a Channel with Bars in Tandem and in Side by Side Arrangements*', International Journal of Numerical Method for Heat and Fluid Flow, Vol. 10, pp. 877 - 895, 2000.
- [5] A. Valencia, '*Turbulent Flow and Heat Transfer in a Channel with a Square Bar Detached from the Wall*', Numerical Heat Transfer, Part A, Vol. 37, pp. 289 - 306, 2000.
- [6] A. Valencia, '*The effects on Heat Transfer of Unsteady Flow Around Two Square Bars Mounted Staggered in a Plane Channel*', International Communications of Heat and Mass Transfer, Vol. 29, N°2, pp. 233 - 242, 2002.
- [7] A. Valencia and M. Cid, '*Turbulent Unsteady Flow and Heat Transfer in Channels with Periodically Mounted Square Bars*', International Journal of Heat and Mass Transfer, Vol. 45, N°8, pp. 1661 - 1673, 2002.
- [8] E.M. Sparrow, J.P. Abraham, and J.C.K. Tong, '*Archival Correlations for Average Heat Transfer Coefficients for Non-Circular and Circular Cylinders and for Spheres in Cross-Flow*', International Journal of Heat and Mass Transfer, Vol. 47, N°24, pp. 5285 - 5296, 2004.
- [9] S. Srikanth, A.K. Dhiman and S. Bijjam, '*Confined Flow and Heat Transfer across a Triangular Cylinder in a Channel*', International Journal of Thermal Sciences, Vol. 49, N°11, pp. 2191 - 2200, 2010.
- [10] H.-W. Wu and H.-W. Ku, '*The optimal Parameters Estimation for Rectangular Cylinders Installed Transversely in the Flow Channel of PEMFC from a Three-dimensional PEMFC Model and the Taguchi Method*', Applied Energy, Vol. 88, N°12, pp. 4879 - 4890, 2011.
- [11] Z. Huang, G. Xi, W. Zhang and S. Wen, '*Mixed Convection Heat Transfer from Confined Tandem Square Cylinders in a Horizontal Channel*', International Journal of Heat and Mass Transfer, Vol. 66, pp. 625 - 631, 2013.
- [13] J. Wang and Y. Zhao, '*Heat and Fluid Flow Characteristics of a Rectangular Channel with a Small Diameter Circular Cylinder as Vortex Generator*', International Journal of Thermal Sciences, Vol. 92, pp. 1
- [12] A. Kumar, A. Dhiman and L. Baranyi, '*CFD Analysis of Power-Law Fluid Flow and Heat Transfer around a Confined Semi-Circular Cylinder*', International Journal of Heat and Mass Transfer, Vol. 82, pp. 159 - 169, 2015.

- [13] J. Wang and Y. Zhao, '*Heat and Fluid Flow Characteristics of a Rectangular Channel with a Small Diameter Circular Cylinder as Vortex Generator*', International Journal of Thermal Sciences, Vol. 92, pp. 1 - 13, 2015.
- [14] B.E. Launder and D.B. Spalding, '*The Numerical Computation of Turbulent Flows*', Computer Methods in Applied Mechanics and Engineering., Vol. 3, pp. 269 -289,1974.
- [15] J.O. Hinze, '*Turbulence*', McGraw-Hill, 1975.
- [16] Fluent 6.3, '*User's Guide*', Centerra Park Lebanon, NH, USA, 2006.
- [17] S.V. Patankar, '*Numerical Heat Transfer and Fluid Flow*', Mc Graw-Hill, New York, 1980.
- [18] J.P. Van Doormaal and G.D. Raithby, '*Enhancements of the Simple Method for Predicting Incompressible Fluid Flows*', Numerical Heat Transfer, Vol. 7, pp. 147 - 163, 1985.
- [19] F. Incropera and P.D. Dewitt, '*Introduction to Heat Transfer*', 5<sup>th</sup> Edition John Wiley and Sons Inc, 2006.
- [20] C.K.G. Lam and K.A. Bremhorst, '*Modified from of the  $k-\epsilon$  Model for Predicting Wall Turbulence*', ASME Journal of Fluids Engineering, Vol. 103, N°3, pp. 456 - 460, 1981.
- [21] H.K. Versteeg and W. Malalasekera, '*An Introduction to Computational Fluid Dynamics, the Finite Volume Method*', Addison Wesley Longman Limited, England, 1995.
- [22] D.C. Wilcox, '*Multiscale Model for Turbulent Flows*', AIAA 24<sup>th</sup> Aerospace Sciences Meeting. American Institute of Aeronautics and Astronautics, 1986.
- [23] F.R. Menter, '*Two-equation Eddy-viscosity Turbulence Models for Engineering Applications*', AIAAJ., Vol. 32, N°8, pp. 1598-1605, 1994.